Wave Propagation in Fractured Poroelastic Media

WCCM, MS170: Advanced Computational Techniques in Geophysical Sciences,

Barcelona, Spain, July 2014

Juan E. Santos[†]

[†] Instituto del Gas y del Petróleo (IGPUBA), UBA, Argentina, and Universidad Nacional de La Plata (UNLP), Argentina and Department of Mathematics, Purdue University, Indiana, USA,

work in collaboration with J. M. Carcione (OGS, Italy) and S. Picotti, R. Martinez Corredor (UNLP).

Fractured media. I

- **Fractures are common in the earth's crust due to different factors, for instance, tectonic stresses and natural or artificial hydraulic fracturing caused by a pressurized fluid.**
- **Seismic wave propagation through fractures and cracks is an important subject in exploration and production geophysics, earthquake seismology and mining.**
- **In geophysical prospecting, reservoir development and CO2 storage in geological formations, knowledge of fracture orientation, densities and sizes is essential since these factors control hydrocarbon production.**

Fractured media. II

- A planar fracture embedded in a Biot background is a particular case of the thin layer problem, when one of the layers is very thin, highly permeable and compliant.
- A Biot medium containing a dense set of aligned fractures behaves as an effective transversely isotropic and viscoelastic (TIV) medium at the macroscale when the predominant wavelength is much larger than the average distance between fractures.
- One important mechanism in Biot media at seismic frequencies is wave-induced fluid flow generated by fast compressional waves at mesoscopic-scale heterogeneities, generating slow diffusion-type Biot waves.

Fractured media. III

- In the context of Numerical Rock Physics, we present and analyze a set of time-harmonic finite element (FE) experiments that take into account the effects of the presence of aligned fractures and interlayer fluid flow occurring at the mesoscale.
- These numerical experiments allow to determine the complex and frequency dependent stiffnesses of the effective TIV medium at the macroscale. They are defined as BVP on representative samples of the fractured material, with boundary conditions associated with compressibility and shear tests, which are solved using the FE method.

Anisotropic poroelasticity. I

- For Biot's media, White et al. (1975) were the first to introduce the mesoscopic-loss mechanism in the framework of Biot's theory.
- For fine layered poroelastic materials, the theories of Gelinsky and Shapiro (GPY, 62, 1997) and Krzikalla and Müller (GPY, 76, 2011) allow to obtain the five complex and frequency-dependent stiffnesses of the equivalent TIV medium.
- To test the model and provide a more general modeling tool, we present a FE upscaling procedure to obtain the complex stiffnesses of the equivalent TIV medium.
- The samples contain mesoscopic-scale heterogeneities due to patchy brine-CO_2 saturation and fractal porosity (fractal frame properties).

TIV media and fine layering. I

Let us consider isotropic fluid-saturated poroelastic layers.

$\mathbf{u}^s(\mathbf{x}), \mathbf{u}^f(\mathbf{x})$ **: time Fourier transform of the displacement vector of the solid and fluid relative to the solid frame, respectively.**

$\mathbf{u} = (\mathbf{u}^s, \mathbf{u}^f)$

$\sigma_{kl}(\mathbf{u}), \mathbf{p}_f(\mathbf{u})$ **: Fourier transform of the total stress and the fluid pressure, respectively.**

$\mathbf{e}(\mathbf{u}_s)$ **the strain tensor of the solid phase.**

On each plane layer n **in a sequence of** N **layers, the frequency-domain stress-strain relations are**

$$\sigma_{kl}(\mathbf{u}) = 2\mu\, e_{kl}(\mathbf{u}^s) + \delta_{kl}\left(\lambda_{_G}\, \nabla\cdot\mathbf{u}^s + \alpha M \nabla\cdot\mathbf{u}^f\right),$$

$$\mathbf{p}_f(\mathbf{u}) = -\alpha M \nabla\cdot\mathbf{u}^s - M\nabla\cdot\mathbf{u}^f.$$

TIV media and fine layering. II

$$\alpha = 1 - \frac{K_m}{K_s}, \quad M = \left[\frac{\alpha - \phi}{K_s} + \frac{\phi}{K_f}\right]^{-1}.$$

$$K_G = K_m + \alpha^2 M, \quad \lambda_G = K_G - \frac{2}{3}\mu,$$

μ: **shear modulus of the dry matrix,**

K_m, Ks, K_f, K_G: **bulk modulus of the dry matrix, the solid grains, the saturant fluid, and the saturated bulk material, respectively.**

Biot's equations in the diffusive range:

$$\nabla \cdot \sigma(\mathbf{u}) = 0,$$
$$\mathrm{i}\omega \frac{\eta}{\kappa} \mathbf{u}^f(\mathbf{x}, \omega) + \nabla p_f(\mathbf{u}) = 0,$$

η, κ **: fluid viscosity and frame permeability, respectively,**

$\omega = 2\pi f$ **: angular frequency**

TIV media and fine layering. III

$\tau_{ij}(\widetilde{\mathbf{u}}_s), \epsilon_{ij}(\widetilde{\mathbf{u}}_s)$: **stress and strain tensor components of the equivalent TIV medium,**

$\widetilde{\mathbf{u}}_s$: **solid displacement vector at the macroscale.**

The stress-strain relations (assuming a closed system ($\nabla \cdot \mathbf{u}_f = 0$))

$$\tau_{11}(\widetilde{\mathbf{u}}_s) = p_{11}\,\epsilon_{11}(\widetilde{\mathbf{u}}_s) + p_{12}\,\epsilon_{22}(\widetilde{\mathbf{u}}_s) + p_{13}\,\epsilon_{33}(\widetilde{\mathbf{u}}_s),$$

$$\tau_{22}(\widetilde{\mathbf{u}}_s) = p_{12}\,\epsilon_{11}(\widetilde{\mathbf{u}}_s) + p_{11}\,\epsilon_{22}(\widetilde{\mathbf{u}}_s) + p_{13}\,\epsilon_{33}(\widetilde{\mathbf{u}}_s),$$

$$\tau_{33}(\widetilde{\mathbf{u}}_s) = p_{13}\,\epsilon_{11}(\widetilde{\mathbf{u}}_s) + p_{13}\,\epsilon_{22}(\widetilde{\mathbf{u}}_s) + p_{33}\,\epsilon_{33}(\widetilde{\mathbf{u}}_s),$$

$$\tau_{23}(\widetilde{\mathbf{u}}_s) = 2\,p_{55}\,\epsilon_{23}(\widetilde{\mathbf{u}}_s), \quad \tau_{13}(\widetilde{\mathbf{u}}_s) = 2\,p_{55}\,\epsilon_{13}(\widetilde{\mathbf{u}}_s),$$

$$\tau_{12}(\widetilde{\mathbf{u}}_s) = 2\,p_{66}\,\epsilon_{12}(\widetilde{\mathbf{u}}_s).$$

This approach provides the complex velocities of the fast modes and takes into account interlayer flow effects..

The harmonic experiments to determine the stiffness coefficients. I

To determine the complex stiffness we solve Biot's equation in the 2D case on a reference square $\Omega = (0, L)^2$ with boundary Γ in the (x_1, x_3)-plane.

Set $\Gamma = \Gamma^L \cup \Gamma^B \cup \Gamma^R \cup \Gamma^T$, where

$$\Gamma^L = \{(x_1, x_3) \in \Gamma : x_1 = 0\}, \quad \Gamma^R = \{(x_1, x_3) \in \Gamma : x_1 = L\},$$

$$\Gamma^B = \{(x_1, x_3) \in \Gamma : x_3 = 0\}, \quad \Gamma^T = \{(x_1, x_3) \in \Gamma : x_3 = L\}.$$

The harmonic experiments to determine the stiffness coefficients. II

The sample is subjected to harmonic compressibility and shear tests described by the following sets of boundary conditions.

$p_{33(\omega)}$:

$$\sigma(\mathbf{u})\boldsymbol{\nu}\cdot\boldsymbol{\nu} = -\Delta P, \quad (x_1, x_3) \in \Gamma^T,$$
$$\sigma(\mathbf{u})\boldsymbol{\nu}\cdot\boldsymbol{\chi} = 0, \quad (x_1, x_3) \in \Gamma$$
$$\mathbf{u}^s\cdot\boldsymbol{\nu} = 0, \quad (x_1, x_3) \in \Gamma^L \cup \Gamma^R \cup \Gamma^B,$$
$$\mathbf{u}^f\cdot\boldsymbol{\nu} = 0, \quad (x_1, x_3) \in \Gamma.$$

$\boldsymbol{\nu}$: the unit outer normal on Γ

$\boldsymbol{\chi}$: a unit tangent on Γ so that $\{\boldsymbol{\nu}, \boldsymbol{\chi}\}$ is an orthonormal system on Γ.

Denote by V the original volume of the sample and by $\Delta V(\omega)$ its (complex) oscillatory volume change.

The harmonic experiments to determine the stiffness coefficients. III

In the quasistatic case

$$\frac{\Delta V(\omega)}{V} = -\frac{\Delta P}{p_{33}(\omega)},$$

Then after computing the average $u_3^{s,T}(\omega)$ **of the vertical displacements on** Γ^T **, we approximate**

$$\Delta V(\omega) \approx L u_3^{s,T}(\omega)$$

which enable us to compute $p_{33}(\omega)$

To determine $p_{11}(\omega)$ **we solve an identical boundary value problem than for** p_{33} **but for a 90**$^{\mathrm{o}}$ **rotated sample.**

The harmonic experiments to determine the stiffness coefficients. IV

$p_{55}(\omega)$: **the boundary conditions are**

$$
\begin{aligned}
&-\boldsymbol{\sigma}(\mathbf{u})\nu = \mathbf{g}, \quad (x_1, x_3) \in \Gamma^T \cup \Gamma^L \cup \Gamma^R, \\
&\mathbf{u}^s = 0, \quad (x_1, x_3) \in \Gamma^B, \\
&\mathbf{u}^f \cdot \boldsymbol{\nu} = 0, \quad (x_1, x_3) \in \Gamma,
\end{aligned}
$$

where

$$
\mathbf{g} = \begin{cases} (0, \Delta G), & (x_1, x_3) \in \Gamma^L, \\ (0, -\Delta G), & (x_1, x_3) \in \Gamma^R, \\ (-\Delta G, 0), & (x_1, x_3) \in \Gamma^T. \end{cases}
$$

The harmonic experiments to determine the stiffness coefficients. V

The change in shape suffered by the sample is

$$\tan[\theta(\omega)] = \frac{\Delta G}{p_{55}(\omega)}. \tag{1}$$

$\theta(\omega)$ **: the angle between the original positions of the lateral boundaries and the location after applying the shear stresses.**

Since

$$\tan[\theta(\omega)] \approx u_1^{s,T}(\omega)/L,$$

where $u_1^{s,T}(\omega)$ **is the average horizontal displacement at** Γ^T**,** $p_{55}(\omega)$ **can be determined from (1).**

To determine $p_{66}(\omega)$ **(shear waves traveling in the** (x_1, x_2) **-plane), we rotate the sample** 90° **and apply the shear test as indicated for** $p_{55}(\omega)$**.**

The harmonic experiments to determine the stiffness coefficients. VI

$p_{13}(\omega)$ **: the boundary conditions are**

$$\boldsymbol{\sigma}(u)\boldsymbol{\nu}\cdot\boldsymbol{\nu} = -\Delta P, \quad (x_1, x_3) \in \Gamma^R \cup \Gamma^T,$$
$$\boldsymbol{\sigma}(u)\boldsymbol{\nu}\cdot\boldsymbol{\chi} = 0, \quad (x_1, x_3) \in \Gamma,$$
$$\mathbf{u}^s\cdot\boldsymbol{\nu} = 0, \quad (x_1, x_3) \in \Gamma^L \cup \Gamma^B, \quad \mathbf{u}^f\cdot\boldsymbol{\nu} = 0, \quad (x_1, x_3) \in \Gamma.$$

In this experiment $\epsilon_{22} = \nabla\cdot u^f = 0$ **, so that**

$$\tau_{11} = p_{11}\epsilon_{11} + p_{13}\epsilon_{33}, \quad \tau_{33} = p_{13}\epsilon_{11} + p_{33}\epsilon_{33},$$

$\epsilon_{11}, \epsilon_{33}$ **: the strain components at the right lateral side and top side of the sample, respectively. Then, since** $\tau_{11} = \tau_{33} = -\Delta P$**,**

$$p_{13}(\omega) = \left(p_{11}\epsilon_{11} - p_{33}\epsilon_{33}\right) / \left(\epsilon_{11} - \epsilon_{33}\right).$$

Schematic representation of the oscillatory compressibility and shear tests in Ω

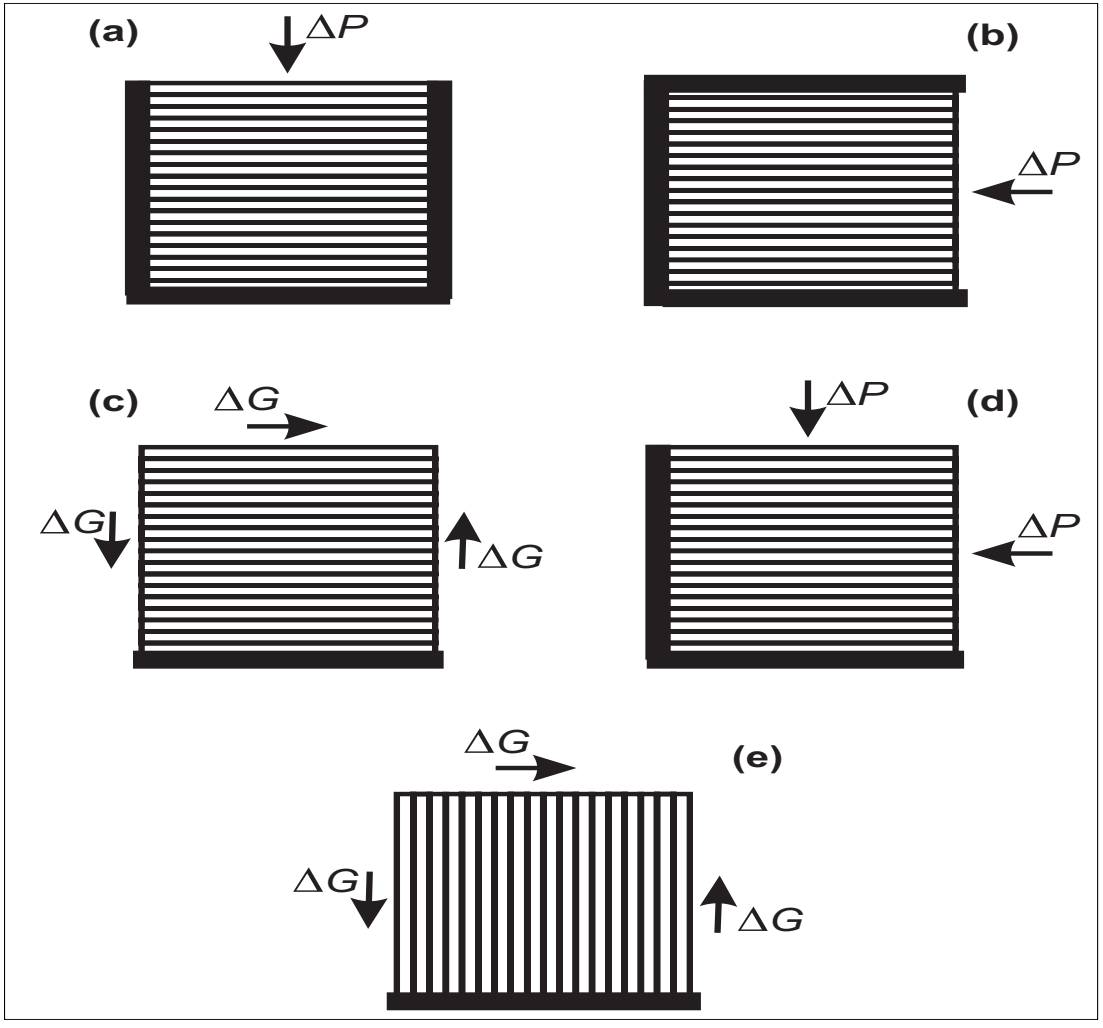

a): p_{33}, b): p_{11}, c): p_{55}, d): p_{13} e): p_{66}

Numerical Examples.

A set of numerical examples consider the following cases for a square poroelastic sample of 160 cm side length and 10 periods of 1 cm fracture, 15 cm background:

- **Case 1: A brine-saturated sample with fractures.**
- **Case 2: A brine-CO_2 patchy saturated sample without fractures.**
- **Case 3: A brine-CO_2 patchy saturated sample with fractures.**
- **Case 4: A brine saturated sample with a fractal frame and fractures.**

The discrete boundary value problems to determine the complex stiffnesses $p_{IJ}(\omega)$ were solved for 30 frequencies using a public domain sparse matrix solver package.
Using relations not included for brevity, the $p_{IJ}(\omega)$'s determine in turn the energy velocities and dissipation coefficients shown in the next figures.

Material Properties of background and fractures.

- **Background and fractures:**
  grain density is $\rho_s = 2650$ **kg/m**^{3}**,**
  bulk modulus is $K_s = 37$ **GPa,**
  shear modulus is $\mu_s = 44$ **GPa.**
- **Background:**
  Porosity is $\phi = 0.25$**, Permeability is** $\kappa = 0.247$ **Darcy,**
  dry bulk modulus is $K_m = 1.17$ **GPa,**
  shear modulus is $\mu = 1.45$ **GPa.**
- **Fractures:**
  Porosity is $\phi = 0.5$**, Permeability is** $\kappa = 4.44$ **Darcy,**
  dry bulk modulus is $K_m = 0.58$ **GPa,**
  shear modulus is $\mu = 0.68$ **GPa.**

Validation. Analytical and numerical solutions for case 1. Dissipation factor of qP waves and qSV waves at 300 Hz

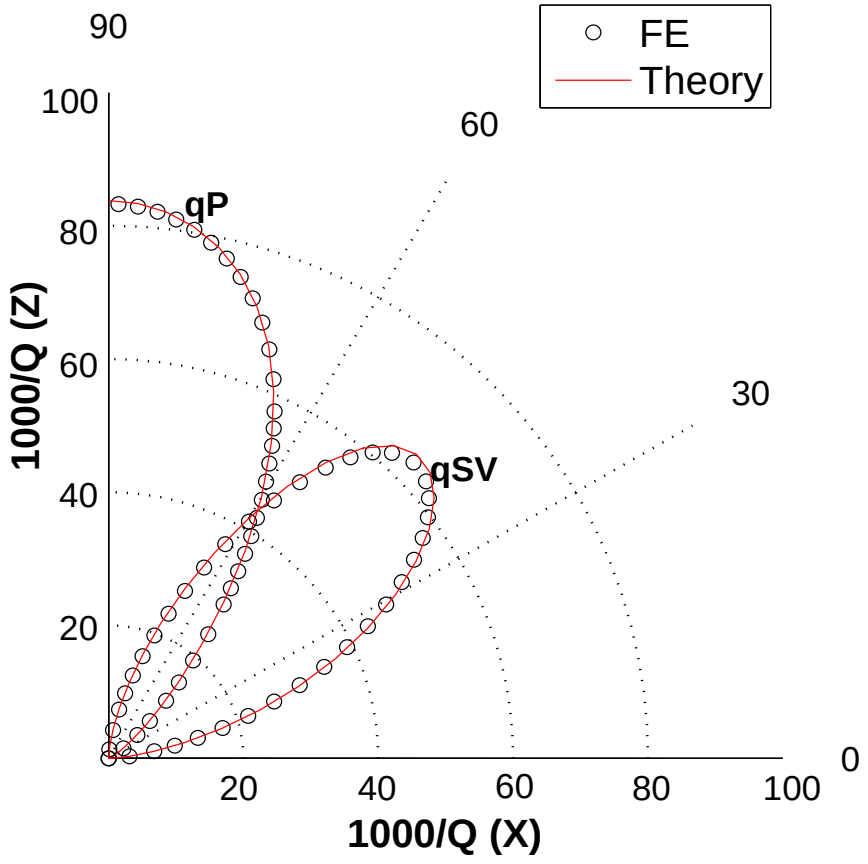

A very good match between the theoretical and numerical results is observed.

Validation. Analytical and numerical solutions for case 1. Energy velocity of qP waves and qSV waves at 300 Hz

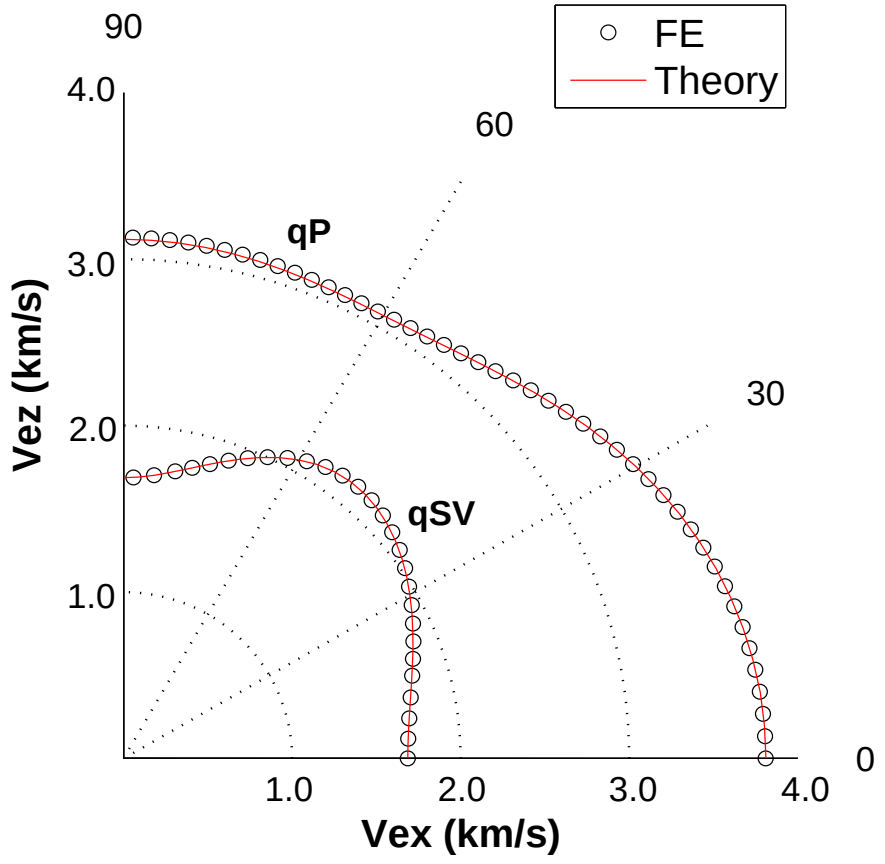

A very good match between the theoretical and numerical results is observed.

Dissipation factors of qP waves at 50 Hz and 300 Hz. Cases 1, 2 and 3

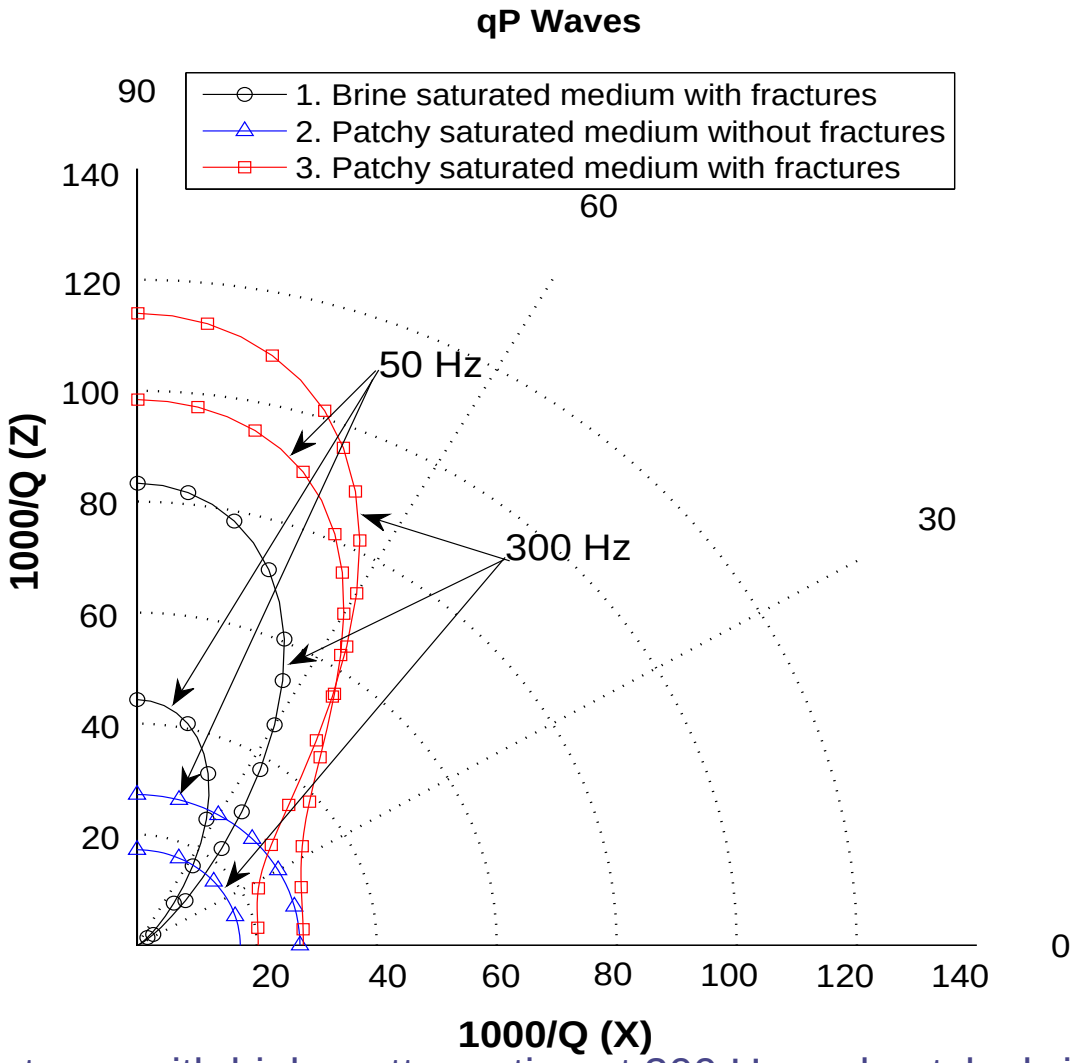

Note strong Q anisotropy, with higher attenuation at 300 Hz and patchy brine-CO_2 saturation.

Energy losses are much higher for angles between 60 and 90 degrees (waves incident normal to the fracture layering)

Energy velocity of qP waves at 50 Hz and 300 Hz. Cases 1, 2 and 3

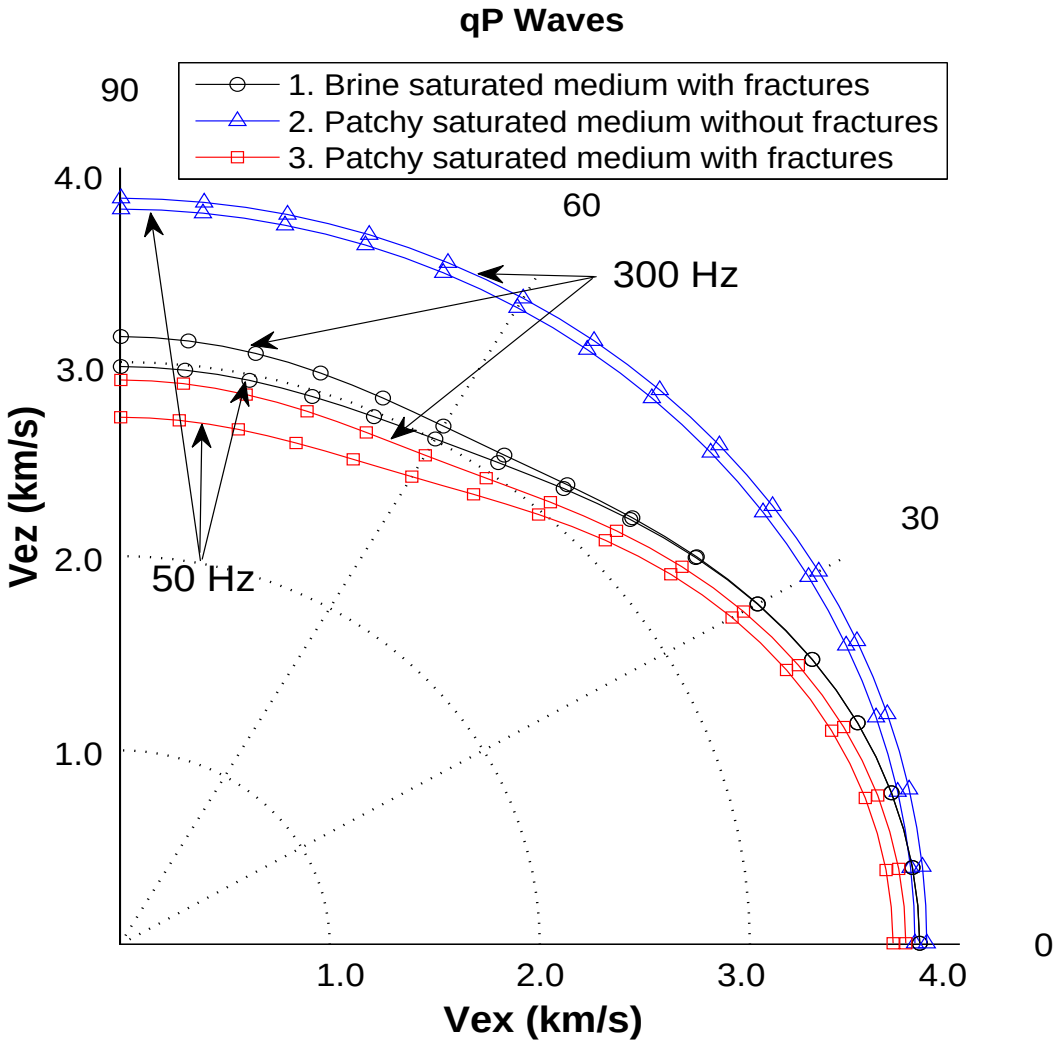

Velocity anisotropy caused by the fractures in cases 1 and 3 is enhanced for the case of patchy saturation, with lower velocities when patches are present. Velocity behaves isotropically in case 2

Fluid pressure distribution at 50 Hz and 300 Hz for case 3 and compressions normal to the fracture layering.

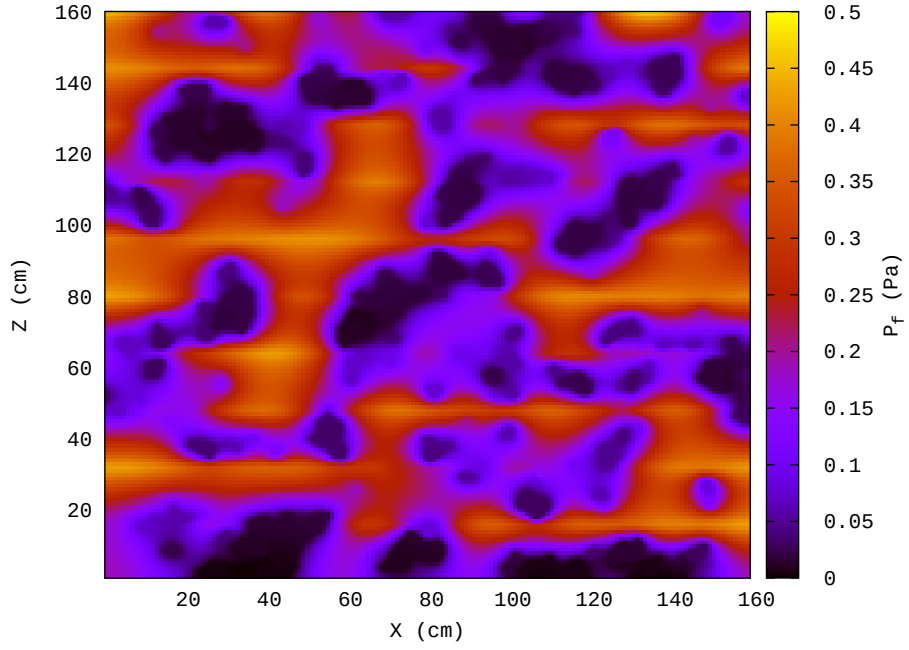

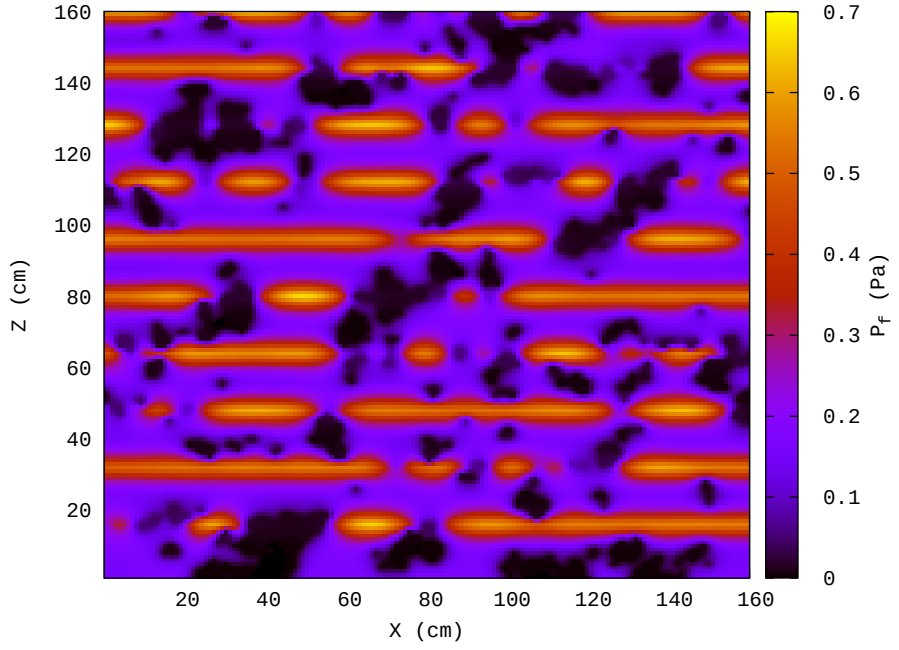

Pressure gradients take their highest values at the fractures (mesoscopic losses), and at 300 Hz remain always higher than at 50 Hz. This explains the higher losses for qP waves at 300 Hz as compared with the 50 Hz experiment observed before.

Relation among different attenuation mechanisms for cases 1, 2 and 3 at 300 Hz

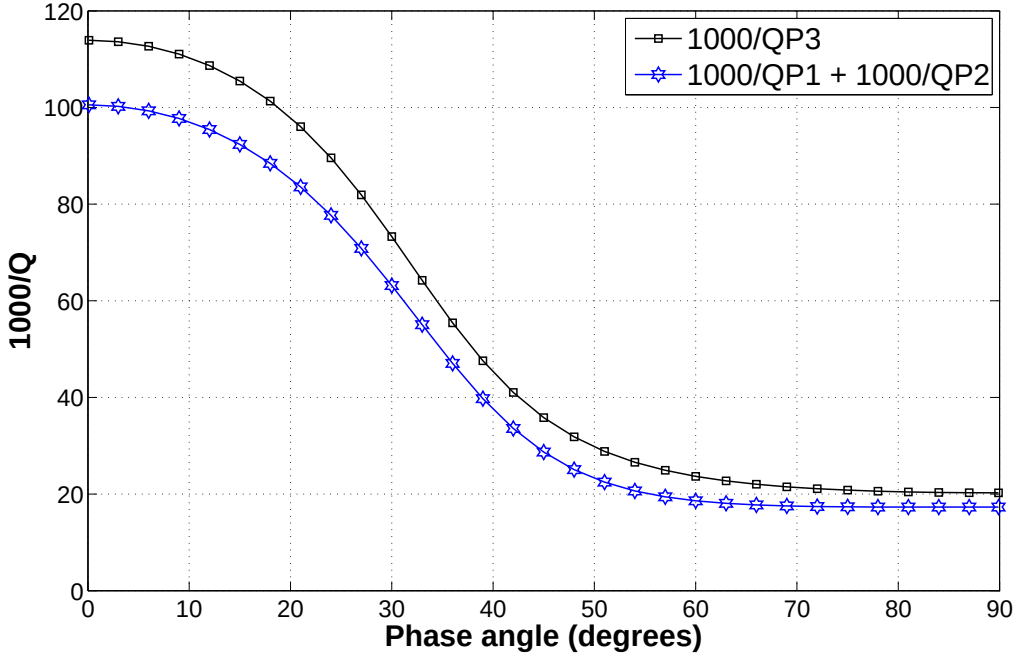

$Q_{\mathrm{P1}}, Q_{\mathrm{P2}}$ and Q_{P3}: qP-quality factors associated with cases 1 (brine with fractures), 2 (patchy without fractures) and 3 (patchy with fractures). Approximate validity of the commonly used approximation

$$Q_{\mathrm{P3}}^{-1} = Q_{\mathrm{P1}}^{-1} + Q_{\mathrm{P2}}^{-1}.$$

Dissipation factors of qSV waves at 50 Hz and 300 Hz. Cases 1, 2 and 3

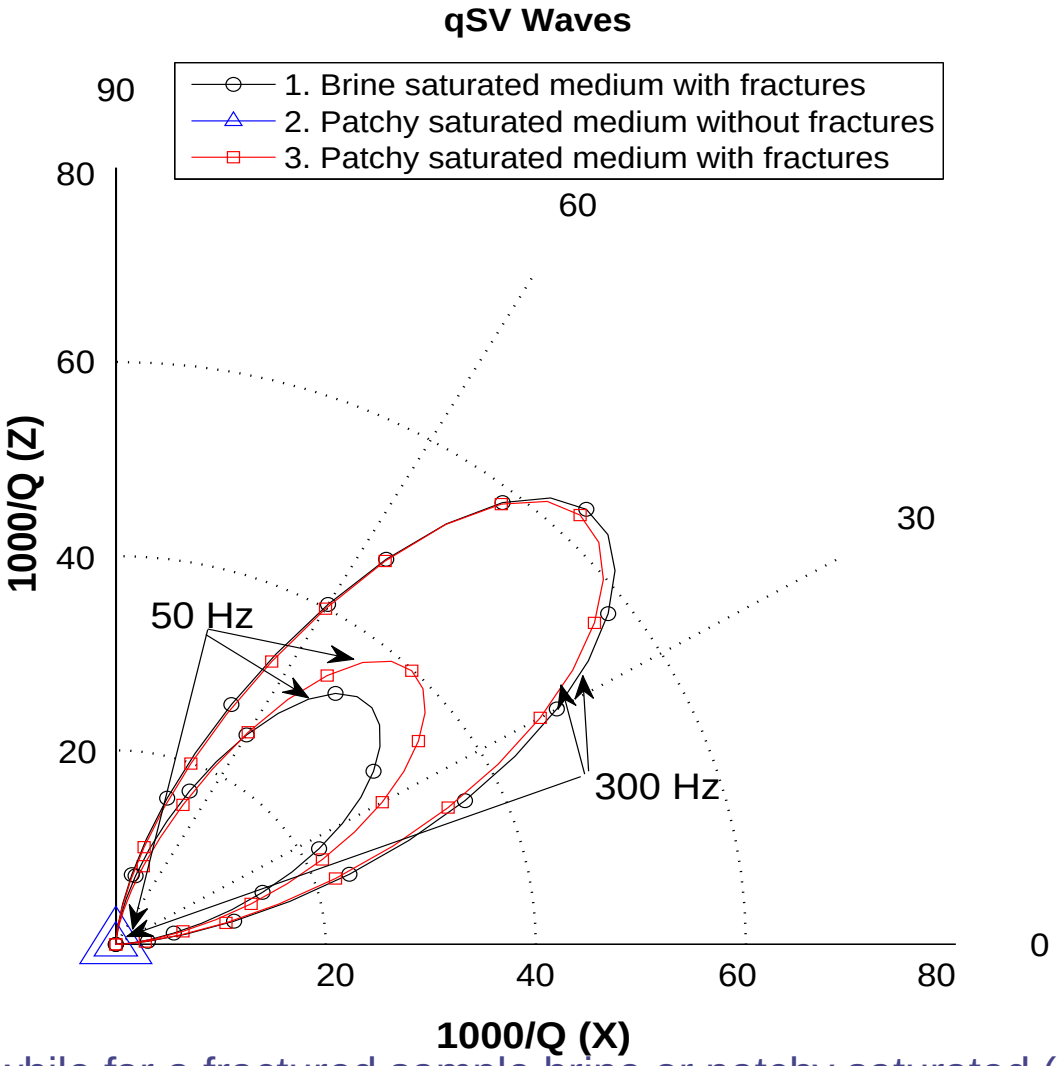

Case 2 is lossless, while for a fractured sample brine or patchy saturated (cases 1 and 3), Q anisotropy is strong for angles between 30 and 60 degrees, with about a 50 % increase in attenuation at 300 Hz with respect to 50 Hz

Energy velocity of qSV and SH waves at 50 Hz. Cases 1, 2 and 3

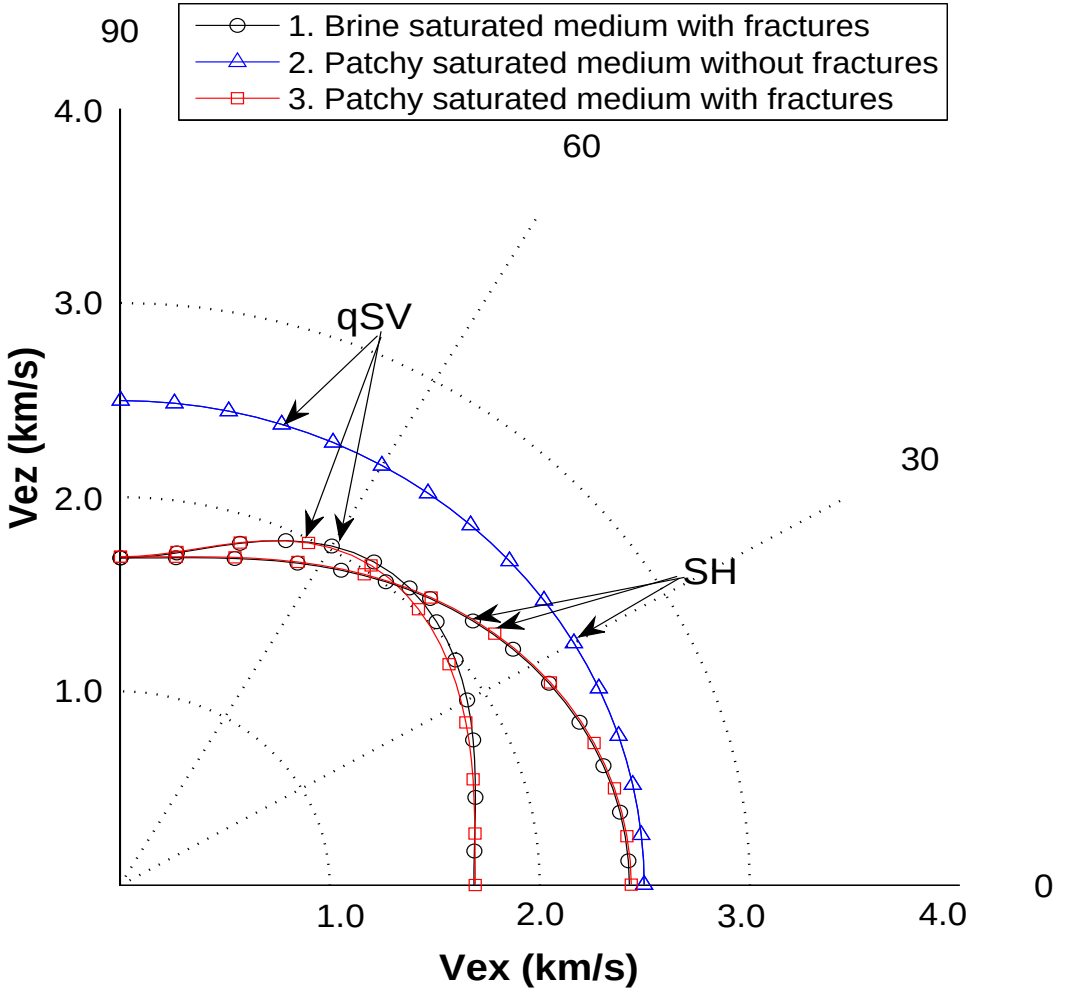

Case 2 shows isotropic velocity for both waves. Velocity anisotropy is observed to be induced by fractures (cases 1 and 3). Patchy saturation does not affect the anisotropic behavior of the velocities. At 300 Hz the behavior is almos identical for qSV was and identical for SH waves.

Dissipation factors of qP and qSV waves for case 3 at 300 Hz as function of CO_2 saturation.

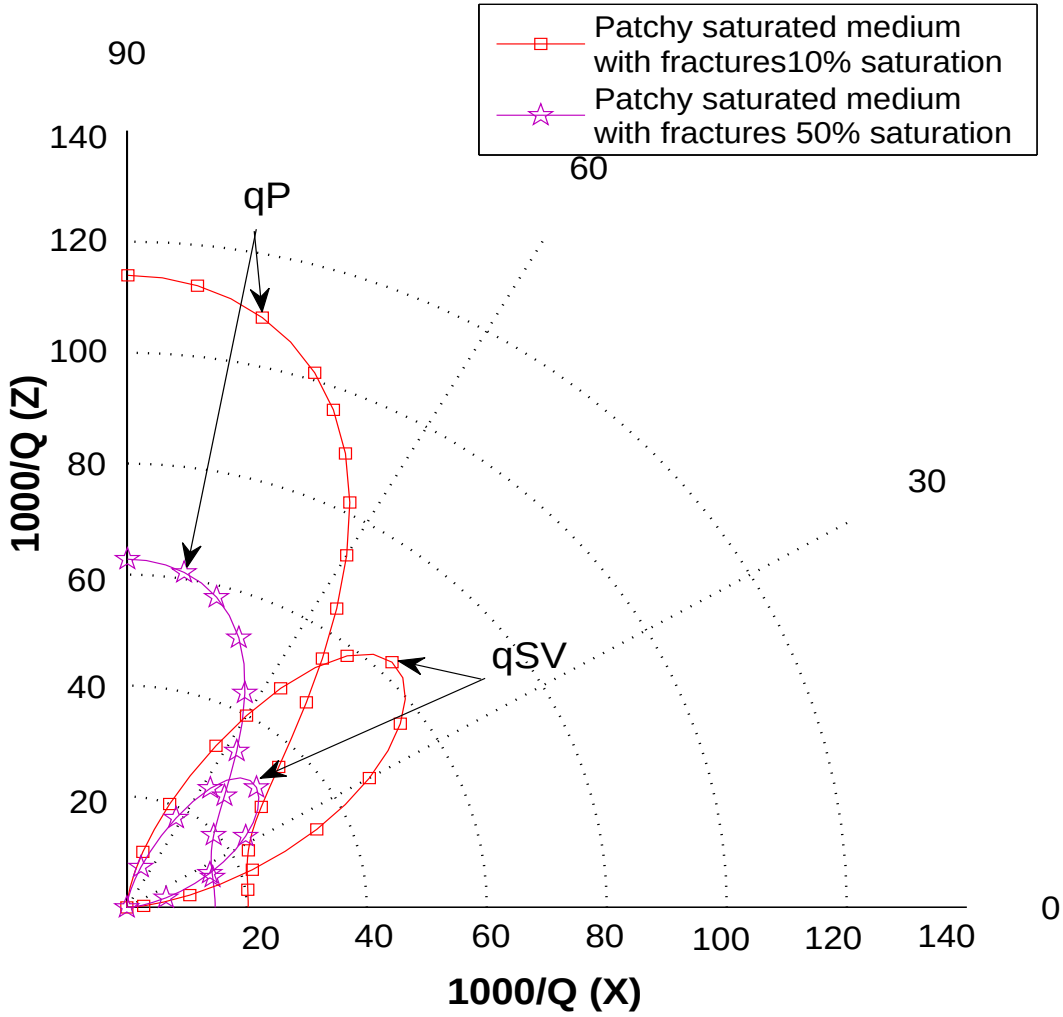

For qP waves, an increase of CO_2 saturation from 10% to 50% induces a strong decrease in attenuation for angles close to the normal orientation of the fractures. For qSV waves the same decrease in attenuation is observed, but for angles between 30 and 60 degrees.

Energy velocities of qP and qSV waves for case 3 at 300 Hz as function of CO_2 saturation.

- **qP energy velocities decrease for increasing CO_2 saturation, with the greater decreases for angles closer to the normal layering of the fractures.**
- **For qSV and SH waves, energy velocities show almost no change between the 10% and 50% CO_2 saturations.**

Dissipation factors for cases 1, 2 and 3 for waves parallel (‘11’ waves) and normal (‘33’ waves) to the fracture layering

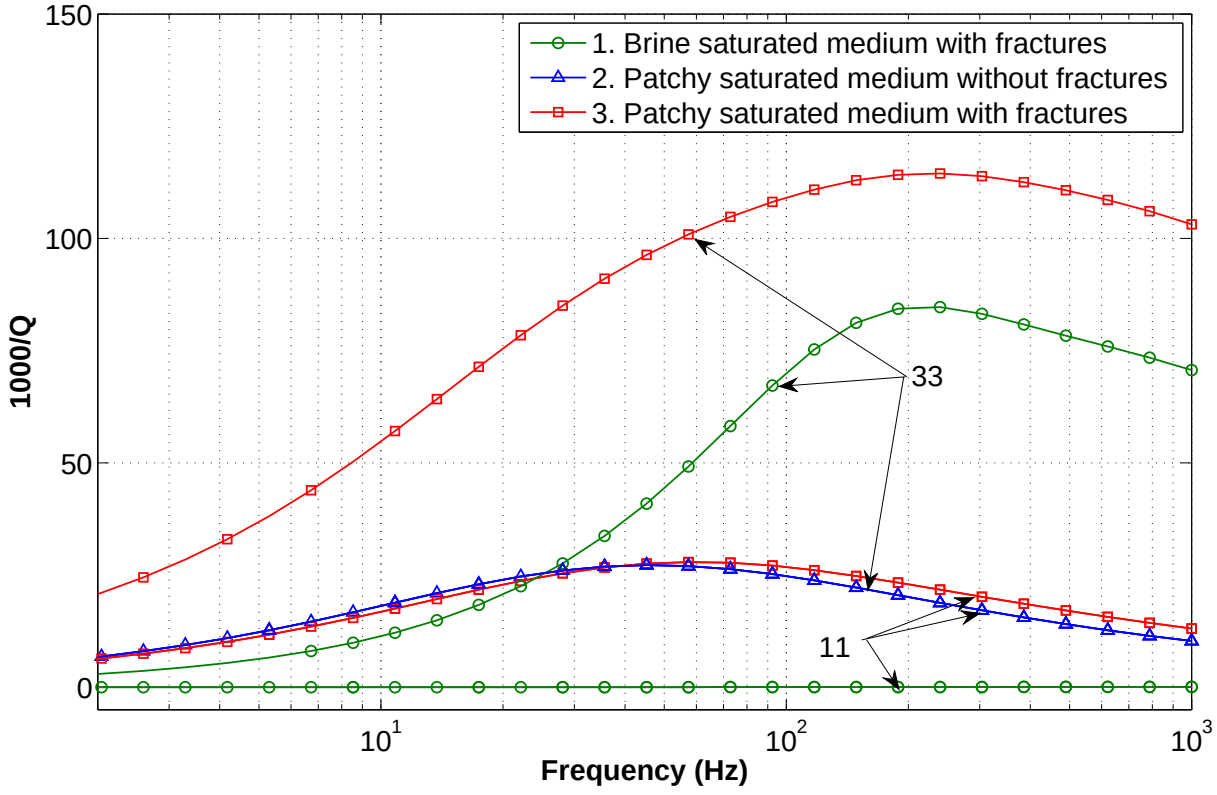

‘11’ waves for case 1 (brine-saturated homogeneous background with fractures) are lossless, while the cases of patchy saturation with and without fractures suffer similar attenuation.

Dissipation factors for cases 1, 2 and 3 for waves parallel (‘11’ waves) and normal (‘33’ waves) to the fracture layering

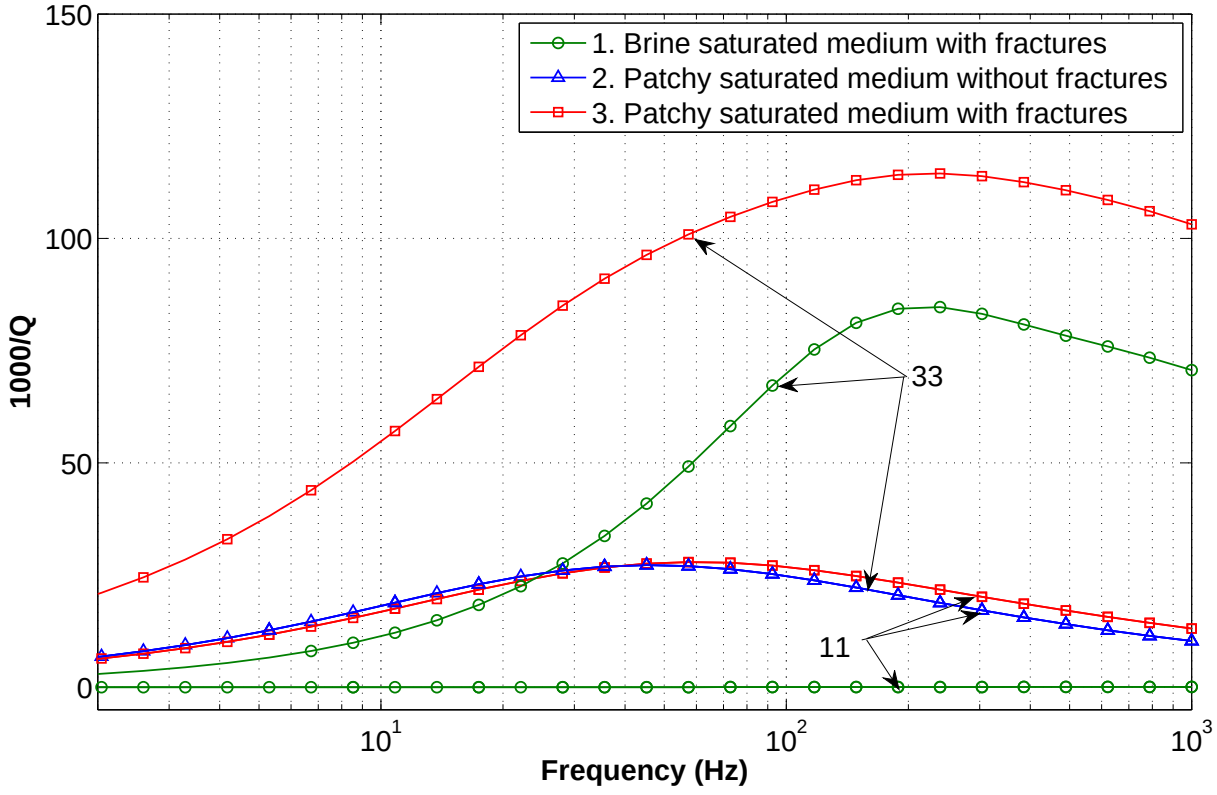

‘11’ waves for case 1 (brine-saturated homogeneous background with fractures) are lossless, while the cases of patchy saturation with and without fractures suffer similar attenuation. ‘33’ show much higher attenuation than those for ‘11’ waves for the three cases.

Velocities for cases 1, 2 and 3 for waves parallel (‘11’ waves) and normal (‘33’ waves) to the fracture layering

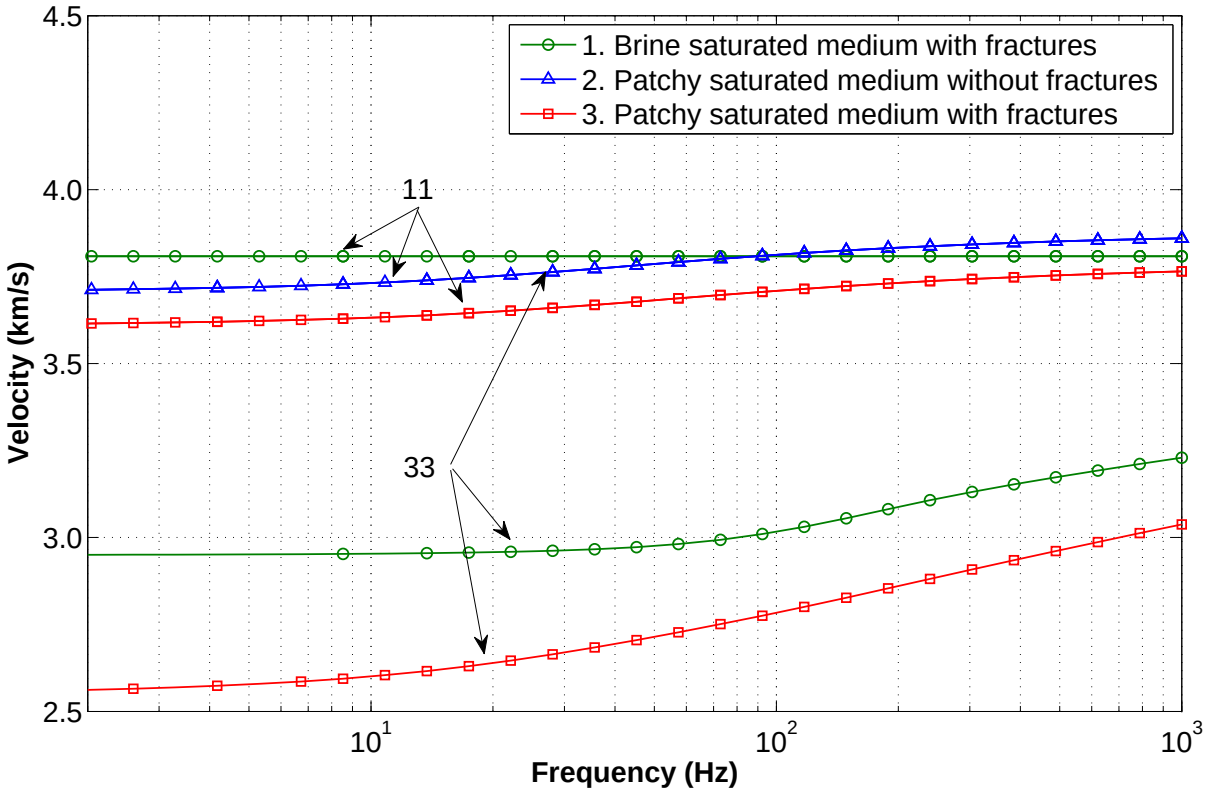

In case 1, ‘11’ velocities are essentially independent of frequency. In the case of patchy saturation with fractures (case 3), velocities are always smaller than in case 1. For ‘33’ waves the presence of fractures induces a noticeable reduction of velocities normal to the fracture plane, either for brine or patchy saturation.

Lamé coefficient λ_G of the brine saturated fractal sample used in case 4

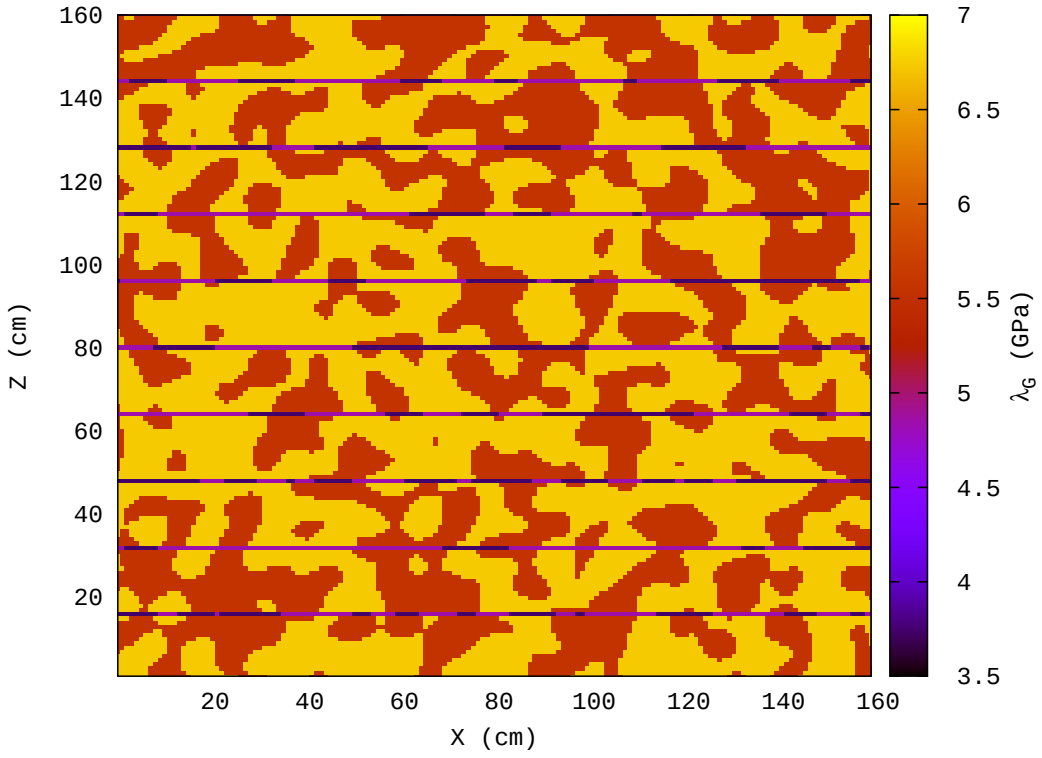

A binary fractal permeability is obtained starting with the relation

$$\log \kappa(x,z) = \langle \log \kappa \rangle + f(x,z)$$

$f(x,z)$: fractal spatial fluctuation of the permeability field, of fractal dimension $D = 2.2$, correlation length 2 cm, and average permeability 0.25 Darcy in the background and 4.44 Darcy in the fractures. Porosity was obtained using the Kozeny-Carman relation.

Dissipation factors of qP and qSV waves at 50 Hz for cases 1 and 4

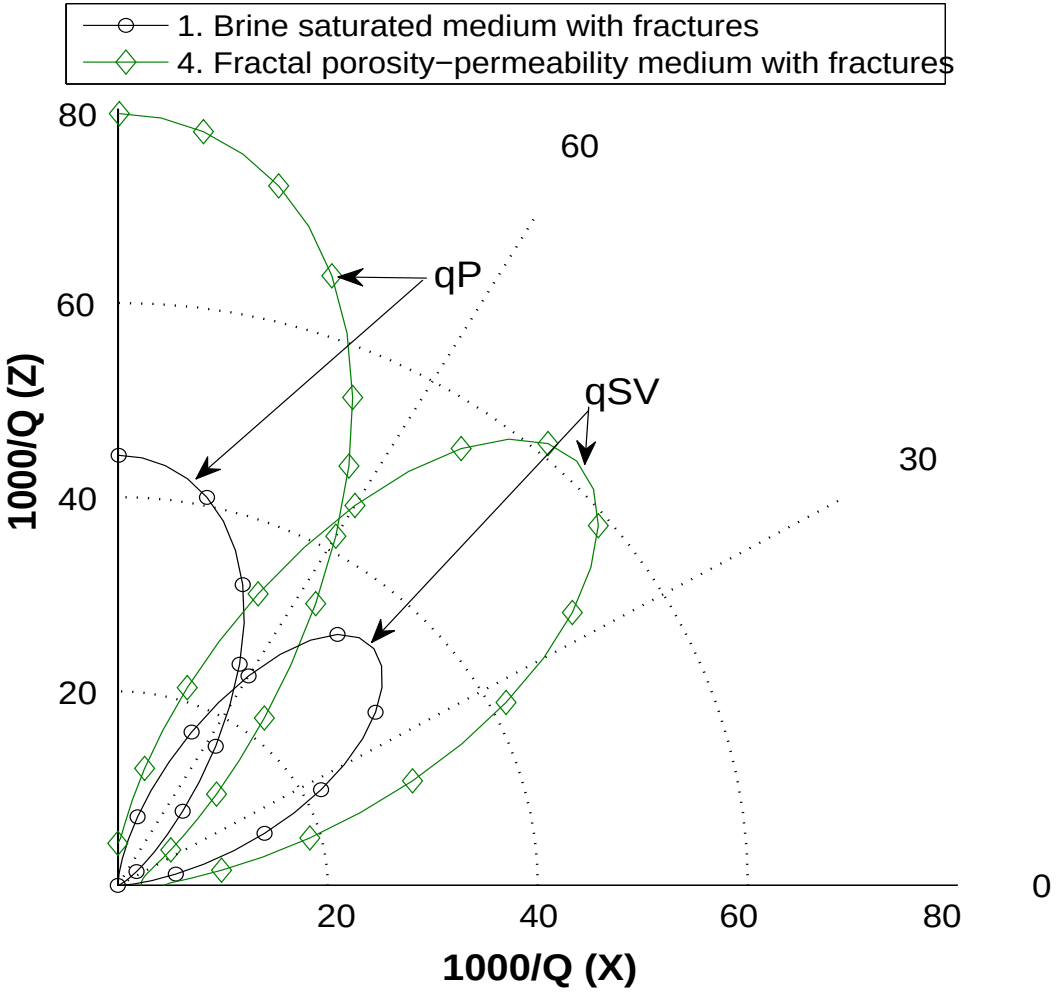

Frame heterogeneities induce a noticeable increase in Q anisotropy for qP waves for angles normal to the fracture plane and for qSV waves for angles between 30 and 60 degrees.

Energy velocity of qP and qSV waves at 50 Hz for cases 1 and 4

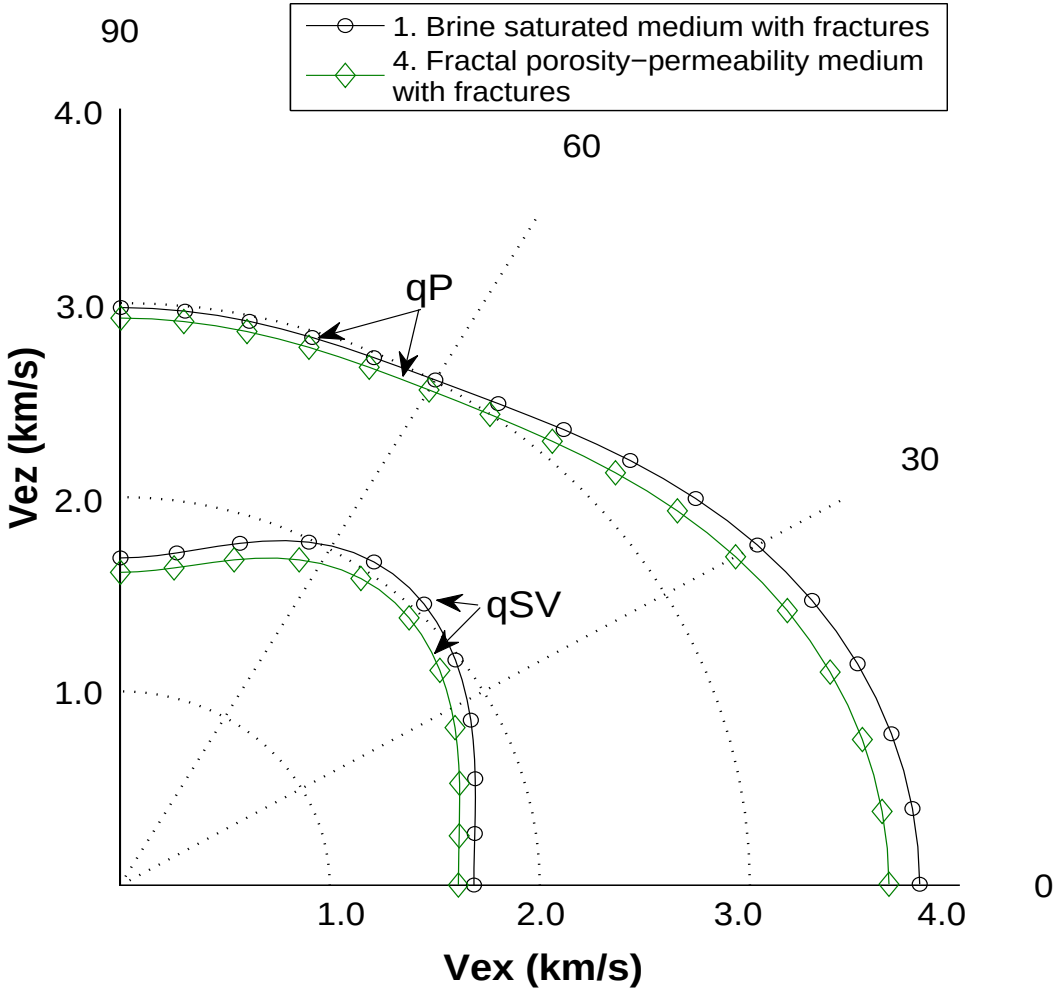

Observe the expected energy velocity reduction in the heterogeneous case, and that velocity anisotropy is less affected by frame heterogeneities than Q anisotropy.

Approximate representation of fractures using boundary conditions. I

Bakulin and Molotov (SEG, 1997) first and later Nakawa and Schoenberg (JASA, 2007) presented a boundary condition to represent approximately fractures in poroelastic media. Consider an horizontal fracture Γ in the (x_1, x_3)- plane separating two half spaces $\Omega^{(1)}, \Omega^{(2)}$ in R^2.

$\boldsymbol{\nu}_{1,2}, \boldsymbol{\chi}_{1,2}$: be the unit outer normal and a unit tangent (oriented counterclockwise) on Γ from $\Omega^{(1)}$ to $\Omega^{(2)}$

$[\mathbf{u}^s], [\mathbf{u}^f]$: jumps of the solid and fluid displacement vectors at Γ:

$$[\mathbf{u}^t] = \left(u^{(t,2)} - \mathbf{u}^{(t,1)}\right)|_\Gamma, \ t = s, f$$

$\mathbf{u}^{(t,1)}$: displacement vector restricted to $\Omega^{(1)}$, and similarly for $u^{(t,2)}$.

Approximate representation of fractures using boundary conditions. II

Boundary conditions on Γ:

$$
\begin{aligned}
[\mathbf{u}_s] \cdot \boldsymbol{\nu}_{1,2} &= \eta_{N_d} \boldsymbol{\sigma}(\mathbf{u}) \boldsymbol{\nu}_{12} \cdot \boldsymbol{\nu}_{12} + \alpha \eta_{N_d} p_f(\mathbf{u}), \quad \Gamma, \\
[\mathbf{u}_s] \cdot \boldsymbol{\chi}_{1,2} &= \eta_T \boldsymbol{\sigma}(u) \boldsymbol{\nu}_{12} \cdot \boldsymbol{\chi}_{12}, \quad \Gamma, \\
[\mathbf{u}_f] \cdot \boldsymbol{\nu}_{1,2} &= -\alpha \eta_{N_d} \boldsymbol{\sigma}(u) \boldsymbol{\nu}_{12} \cdot \boldsymbol{\nu}_{12} - \frac{\alpha \eta_{N_d}}{\widetilde{B}} p_f(\mathbf{u}) \quad \Gamma.
\end{aligned}
$$

η_{N_d} **: Dry normal compliance (m/Pa)**

η_T **: shear compliance (m/Pa)**

$$
\widetilde{B} = \alpha \frac{M}{H_G}, \qquad H_G = K_G + \frac{4}{3}\mu
$$

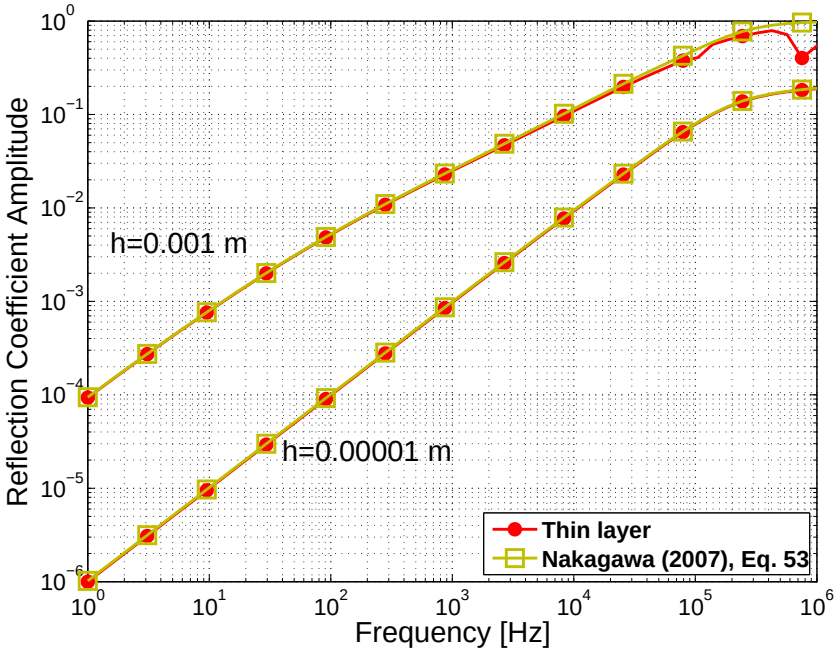

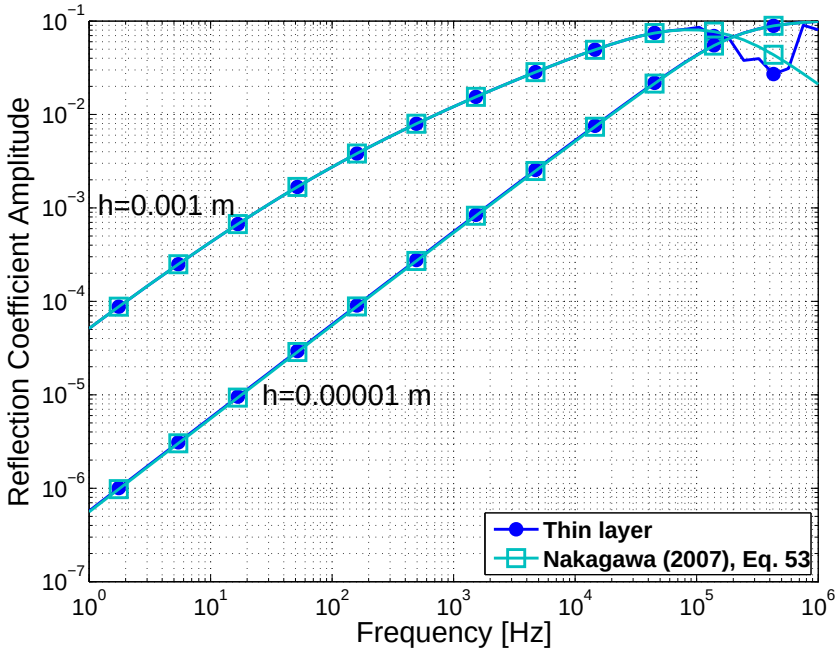

P1-reflection coefficient (left), P2-reflection coefficient (right). Incident wave is a P1-wave of normal incidence to the fracture layering. Fracture aperture h is , h =0.001 m and h =0.00001 m.

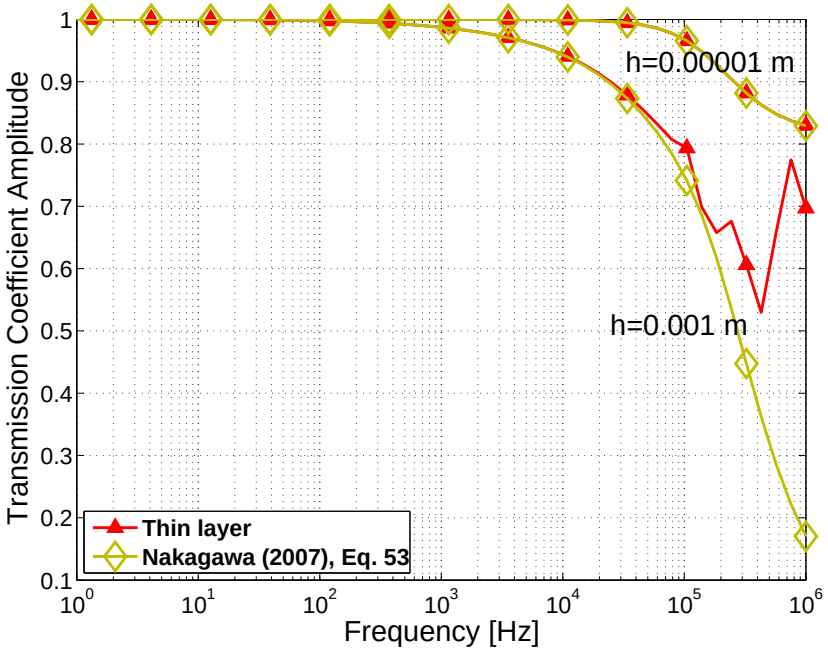

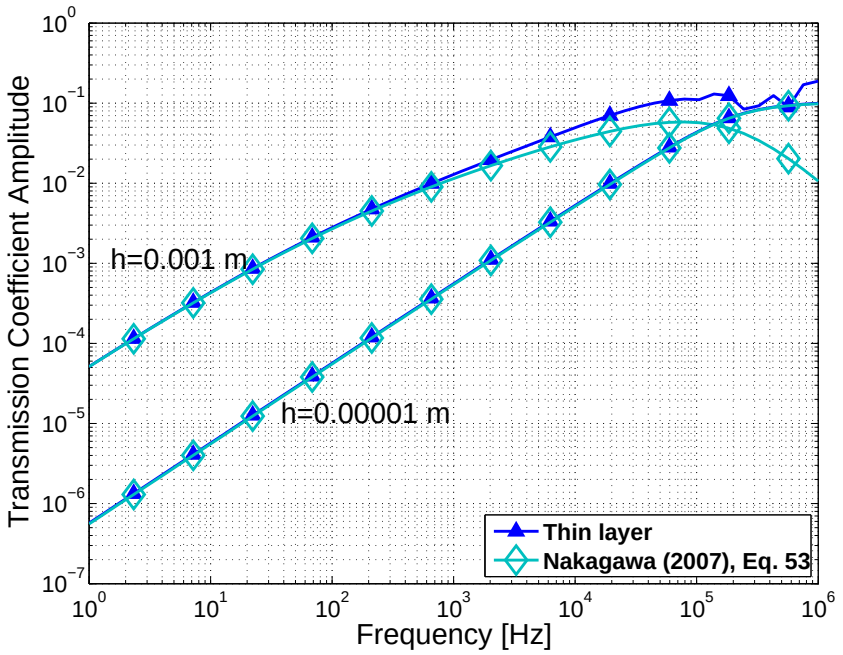

P1-transmission coefficient (left), P2-transmission coefficient (right). Incident wave is a P1-wave of normal incidence to the fracture layering. Fracture aperture h is , h =0.001 m and h =0.00001 m.

Conclusions

- We employed the FEM to determine the complex and frequency-dependent stiffnesses of a VTI homogeneous medium equivalent to a fluid-saturated poroelastic material containing a dense set of planar fractures.
- Fractures induce anisotropy and the P-S coupling generates losses in the shear waves as well.
- Fractures were modeled as very thin highly permeable poroelastic layers of negligible frame moduli.
- Velocity and attenuation anisotropy is observed in the qP and qSV wave modes, with attenuation stronger for the patchy saturated cases. the SH wave is lossless because it is a pure mode in TI media, but shows velocity anisotropy.
- Thanks for your attention !!!!!.